

Synthesis of nanocomposites using glasses and mica as templates

D CHAKRAVORTY*, S BASU, B N PAL[†], P K MUKHERJEE^{††}, B GHOSH, K CHATTERJEE[#], A BOSE, S BHATTACHARYA and A BANERJEE[§]

DST Unit on Nano Science and MLS Professor's Unit, Indian Association for the Cultivation of Science, Kolkata 700 032, India

[†]Department of Materials Science and Engineering, Johns Hopkins University, Maryland, USA

^{††}Department of Physics, Durgapur Government College, Durgapur 713 214, India

[#]Department of Physics, Vidyasagar University, Midnapore 721 102, India

[§]Chemistry Division, Indian Institute of Chemical Biology, Kolkata 700 032, India

Abstract. Various nanocomposites were synthesized using either a silica-based glass or mica crystallites as the medium. In some cases by an oxidation or a sulfidation treatment a core-shell nanostructure could be generated. Iron–iron oxide core-shell structured nanocomposites exhibited excellent humidity sensing behaviour. Gold–gold sulfide core-shell nanorods exhibited a number of optical absorption peaks which arose because of their structural characteristics. Nanoparticles of silver and silver oxide could be aligned in a polymethyl-methacrylate film by an a.c. electric field of 1 MHz frequency. The composites showed large sensitivity to relative humidity. Lead sulfide nanowires of diameter, 1–2 nm, were grown within the nanochannels of Na-4 mica. These exhibited a semiconductor to metal transition at around 300 K. This arose because of high pressure generated on the nanowires. Copper sulfide nanowires grown within the Na-4 mica channels showed metallic behaviour. Silver core–silver orthosilicate shell nanostructures developed within a silicate glass medium showed discontinuous changes in resistivity at some specific temperatures. This was explained as arising due to excitation of Lamb modes at certain pressures generated because of thermal expansion mismatch of the core and the shell phases. Optical properties of iron core–iron oxide shell nanocomposites when analysed by effective medium theory led to the result of a metal non-metal transition for particle diameters below a critical value. Similar results were obtained from optical absorption data of silver nanoparticles grown in a tetrapeptide solution.

Keywords. Synthesis; nanocomposites; glasses; mica.

1. Introduction

Nanocomposites are materials in which a phase with nanoscale dimensions is dispersed within a matrix. A wide variety of nanocomposites have been studied in recent years (Watt *et al* 2005; Ng *et al* 2006; Dutta *et al* 2006; Park and Park 2006; Kesanli *et al* 2006). These systems have acquired significance because of interesting physical properties exhibited by them. Various physical and chemical techniques have been used to synthesize these materials. We have synthesized a number of nanocomposites using either a silica-based glass or a mica structure as the medium. In most cases the nanosized phase consisted of a metal. By suitable oxidation of the composite a core-shell nanostructure was also developed in them. The materials exhibited interesting electrical and optical properties. In some cases, by a suitable choice of the core and the shell phase high pressure could be generated in the nanoscale regions of the composites. This gave rise to unusual behaviour. In this paper, we review the systems studied so far and delineate the properties measured.

2. Experimental

2.1 Nanocomposites with iron–iron oxide core-shell structure

The composites were prepared by first growing iron nanoparticles within a silica based gel by using an electro-deposition technique (Banerjee *et al* 1999). A shell of Fe₃O₄ was then formed around the iron nanoparticles by subjecting the composite to an oxidation treatment.

The composition of the gel to be prepared was chosen as 40 Fe(NO₃)₃ and 60SiO₂. The precursors used were Fe(NO₃)₃·9H₂O and Si(OC₂H₅)₄, respectively. A solution was prepared by dissolving the required amount of Fe(NO₃)₃ in distilled water and ethyl alcohol. The solution was stirred by a magnetic stirrer. A second solution was made by dissolving a calculated amount of Si(OC₂H₅)₄ in distilled water and ethyl alcohol. The above solutions were mixed and stirred for 1 h and the pH value was maintained at 4. Cleaned microscope slides of dimension 2 cm × 2 cm × 1 mm were dipped into the sol and drawn at a speed of 1 mm/s. The slides were dried under ordinary atmosphere for a few hours. Films of thickness around 4 μm were ob-

*Author for correspondence (mlsdc@iacs.res.in)

tained which were transparent. Two silver electrodes (Acheson Colloiden B.V. Holland) were painted on the film surface at a separation of 2 mm. A d.c. voltage of 5 V was applied between the electrodes for around 30 s at room temperature. The formation of metallic filaments was indicated by a sudden increase of current to a value of ~ 1 mA. The specimens were then subjected to an oxidation treatment by heating them to a temperature of 400 K for a period varying from 1–4 h.

The resultant structure was studied by a Leitz Laborlux 18 Pol S optical microscope in the transmission mode. The microstructure of the electrodeposited nanocomposites was investigated by a JEOL 2010 transmission electron microscope.

D.C. electrical resistances of different specimens were measured by a Keithley 617 Electrometer.

Humidity sensing behaviour of these nanocomposites was studied by subjecting them to nitrogen gas flow whose moisture content could be varied by passing it through either a P_2O_5 guard tube or a water container. The relative humidity (RH) value was measured by a Barigo Hygrometer (made in Germany).

2.2 Gold–gold sulfide core–shell structured nanorods

Gold nanorods were, first of all, grown by an electrodeposition technique using polycarbonate membranes as templates (Chatterjee *et al* 2006). The membranes with pore diameter, 100 nm and thickness, 1 μ m (supplied by Whatman, Nuclepore, Clifton, NJ, USA) were painted on one surface by a silver paste (supplied by Acheson Colloiden B. V. Holland, The Netherlands) which acted as the cathode. The experimental arrangement used is shown in figure 6. Tetrachloroauric acid ($HAuCl_4 \cdot xH_2O$) was used as the electrolyte and a gold plate used as the anode.

A d.c. voltage of 1.5 V was applied to the electrolytic cell for 5 min. In the process gold nanorods were formed. The polycarbonate film containing gold nanorods was dissolved in chloroform. The resulting solution was mixed with 2 mg thiourea [$(NH_2)_2CS$]. A few drops of ammoniacal solution were added to the former and it was subjected to a heat treatment at 343 K. As a result the gold nanorods were coated with Au_2S . The microstructure of samples both prior to and after the sulfidation treatment were investigated by a JEOL 2010 transmission electron microscope.

For optical property measurements, Au_2S coated gold nanorods dispersed in chloroform were mounted in the specimen chamber of a UV-2101 PC ultraviolet-visible scanning spectrophotometer (Japan). The absorption spectra were recorded by keeping a chloroform containing dissolved polycarbonate film at the reference beam position.

2.3 Aligned binary system of nanoparticles in a polymer film

The approach was to first prepare nanoparticles of Ag_2O and Ag, respectively and then a solution containing these particles was subjected to an a.c. electric field.

A solution was prepared by dissolving 1 g of analytical grade silver nitrate in 40 c.c. distilled water. A second solution was made by dissolving 0.117 g of NaOH pellet in 20 c.c. distilled water. The pH of the latter solution was ~ 10 . One drop of NaOH solution was added to the first solution and the mixture was stirred vigorously for a few minutes. This precipitated Ag_2O . Ultrafine particles of Ag_2O were obtained by filtering the solution through a Whatman filter paper. A reasonable amount of Ag_2O was extracted by repeating the process several times on the filtrate. After drying the precipitate in vacuum, the Ag_2O particles were heated at 540 K for 1 h. Due to dissociation of Ag_2O to Ag and O_2 at temperatures above 500 K ultrafine silver particles were obtained by the above heat treatment. Particle sizes of the powders (both Ag_2O and Ag) were characterized by a JEM 2010 transmission electron microscope. Next a polymethylmethacrylate (PMMA) solution was made in acetonitrile and a mixture (weighing 4 mg) containing equal amounts of Ag and Ag_2O was poured into the same. The solution was subjected to sonication. Two silver paint electrodes obtained from B. V. Colloiden, Netherlands, were applied on a glass slide at a separation of 1 mm and a few drops of the polymer solution containing Ag and Ag_2O nanoparticles were placed in between. A.C. electric field at frequencies in the range 200 Hz to 1 MHz was applied across the electrodes. Acetonitrile evaporated within 30 s and a stable polymer film formed with specific patterns of the binary nanoparticles.

A Hitachi S-415A Scanning Electron Microscope was used to study the microstructure. D.C. electrical resistances were measured over the temperature range 270–630 K by a Keithley 617 electrometer.

2.4 Lead sulfide nanowires grown in mica channels

The channels within a high-charge density sodium fluorophlogopite mica channels of chemical composition, $Na_4Mg_6Al_4Si_4O_{26}F_{4 \cdot x}H_2O$ (Kodama and Komarneni 1999), were used to grow PbS nanowires of diameter, ~ 1.2 nm.

Mica of the above mentioned composition is commonly referred to as Na-4 mica. This was prepared by a sol–gel method. The chemicals used were $Al(NO_3)_3 \cdot 9H_2O$, $Mg(NO_3)_2 \cdot 6H_2O$ and $Si(OC_2H_5)_4$. The latter were dissolved in C_2H_5OH and the solution was stirred for 3 h. The amounts of the compounds were chosen such that the final composition would be $MgO \cdot Al_2O_3 \cdot 2SiO_2$. The gel was dried at 373 K and the calcination done at 748 K for 12 h. The gel powder was mixed thoroughly with an equal amount of NaF powder. The mixture was subjected

to a heat treatment at 1163 K for 18 h in a platinum crucible. After washing the reaction products with deionized water and then with saturated boric acid they were washed with 1 M NaCl to saturate all exchange sites with Na^+ . After subsequent washing with deionized water the solid was dried at 333 K for 3 days. 2 g of Na-4 mica powder was then immersed into 25 cc of 0.4 (M) $\text{Pb}(\text{NO}_3)_2$ to which 0.5 M NaCl solution was added. This brought about an ion exchange reaction of the type $\text{Pb}^{2+} \leftrightarrow 2\text{Na}^+$ which continued for a period of 4 weeks at 303 K. After separating the ion exchanged powder from the solution by a centrifuge, it was subjected to a heat treatment in H_2S at 673 K for 1 h. This produced PbS wires within the Na-4 mica channels.

The microstructure of the samples was investigated by a JEOL Model JEM 2010 transmission electron microscope.

Electrical measurements were carried out on cold compacted specimens using a pressure of 20 tons/cm² – the specimens having a diameter, 1 cm and thickness, 1 mm. Before d.c. measurement, the specimens were sintered at 973 K for 1 h in a nitrogen atmosphere. Silver paste supplied by B. V. Colloiden, The Netherlands, was used as electrodes. D.C. resistance at different temperatures were measured by Keithley 617 Electrometer. Dielectric properties were measured by a Hewlett Packard Impedance Analyser (HP4192A).

2.5 Copper sulfide nanowires grown within Na-4 nanochannels

Na-4 mica channels were exploited to grow wires of copper sulfide.

Na-4 mica was first prepared by following the procedure described in the previous section. 2 g of the gel powder was immersed in a solution consisting of 0.4 M $\text{CuCl}_2 \cdot 2\text{H}_2\text{O}$ and 0.5 M NaCl. This brought about an ion exchange reaction $\text{Cu}^{2+} \leftrightarrow 2\text{Na}^+$. The reaction was allowed to take place over a period of 4 weeks at 303 K. After separating the ion exchanged powder from the solution by a centrifuge the former was subjected to heat treatment at 673 K for 1 h in H_2S atmosphere. This led to the formation of copper sulfide nanowires within the crystal channels of Na-4 mica.

The procedures for microstructural studies, d.c. resistance and dielectric measurements were identical to those described in the previous section.

2.6 Nanocomposites with silver core–silver orthosilicate shell structures

A silicate glass with suitable composition was chosen to first of all grow nanoparticles of metallic silver which were interconnected. After suitable heat treatment a crystalline phase viz. silver orthosilicate, was grown around

the silver nuclei. With this system it was possible to study the effect of high pressure on the ionic conductivity of the nano-shell comprising of silver orthosilicate (Ghosh *et al* 2004).

Glasses of compositions, 15Na₂O, 15Li₂O, 12CaO, 3Al₂O₃, 55SiO₂, were prepared by melting a mixture of appropriate chemicals and then pouring it on a brass mould at room temperature. Glass particles of size, ~5 μm, were obtained after grinding the quenched glass pieces. The former were immersed in a molten bath of silver nitrate at 583 K for 6 h to bring about ion exchange of the type $\text{Li} \leftrightarrow \text{Ag}^+$ and $\text{Na}^+ \leftrightarrow \text{Ag}^+$, respectively. The treated powder was reduced in hydrogen at 673 K for 30 min. Silver particles were formed in the glass by this step. Electrical measurement carried out on a cold compacted pellet of the reduced powder showed metallic conduction confirming percolation of the silver nanoparticles. The glass powder prepared as above was subjected to a two-stage heat treatment, viz. at 833 K and 993 K, respectively for different periods to nucleate and grow the silver orthosilicate phase.

The microstructural and electrical studies were carried out by methods delineated in previous sections.

2.7 Nanocomposites with iron–iron oxide core-shell structures

Iron nanoparticles were first grown within a gel-derived silicate glass and then by oxidation treatment an iron oxide shell was formed (Basu and Chakravorty 2006).

The target gel composition was 55Fe₂O₃·45SiO₂. The precursor chemicals were FeCl₃ and Si(OC₂H₅)₄. The sol was prepared by mixing weighed amounts of chemicals in ethyl alcohol, distilled water and Si(OC₂H₅)₄. 1 cc of HCl was added. This was allowed to gel for a period of two weeks. The gel was subjected to a reduction treatment in hydrogen at 923 K for 30 min. The powders were then heated in ordinary atmosphere at temperatures in the range 573–973 K for 30 min.

The microstructural studies were carried out by a JEOL2010 transmission electron microscope. Optical absorption spectra were measured by a UV-2101 PC UV-VIS scanning spectrophotometer of Shimadzu-make after dispersing the nanocomposite powders in ethyl alcohol in a test tube.

2.8 Silver nanoparticles grown in an oligopeptide

A water-soluble tetrapeptide solution was used for making silver nanoparticles (Bhattacharya *et al* 2006).

The precursors used were silver nitrate, tetrapeptide and methanol. Preparation of tetrapeptide is described elsewhere (Bodanszky and Bodanszky 1984). Two solutions were prepared, one of tetrapeptide in methanol and water and the other of silver nitrate in methanol and water.

The first solution was then added to the second one under stirring in a dark chamber. The pH of the solution was adjusted to ~ 8 by suitable addition of NaOH solution. Colloidal silver particles were produced due to oxidation of the tyrosine residues of the tetrapeptide.

The microstructural and optical absorption studies were carried out by the procedure described in previous sections.

3. Results and discussion

3.1 Iron-iron oxide core-shell structure

In figure 1 is shown an optical micrograph of a gel sample in which iron metal was grown with a fractal structure by application of a d.c. voltage of 5 V and subsequent oxidation treatment was given at 400 K for 2 h. The fractal dimension was calculated to be 1.82 (Banerjee *et al* 1999). This has been ascribed to the generalized-diffusion-limited-aggregation model (Matshushita *et al* 1986).

Figure 2 shows the transmission electron micrograph for the specimen above. It is evident that the fractal structure is comprised of nanosized particles. From the distribution of particle sizes, a median diameter of 10 nm was extracted. Figure 3 shows the core-shell nanostructure of the particles. From the electron diffraction pattern of these particles the interplanar spacings were calculated. The latter confirmed that the core and the shell were made up of Fe and Fe_3O_4 , respectively (Pal *et al* 2005a).

Figure 4 gives the variation of surface resistivity of a specimen (subjected to a 2 h oxidation treatment) as a

function of inverse temperature. The electrical conduction evidently is controlled by the Fe_3O_4 shell. The latter is known to contain both Fe^{2+} and Fe^{3+} ions. Hence a small polaron conduction model (Mott 1968) was found to be operative in this system. In this model resistivity, ρ , is given by

$$\rho = \frac{kTR}{v_0 e^2 c(1-c)} \exp(2\alpha R) \exp\left(\frac{W}{kT}\right), \quad (1)$$

where k is the Boltzmann constant, T the temperature, R the intersite separation, v_0 the optical phonon frequency,

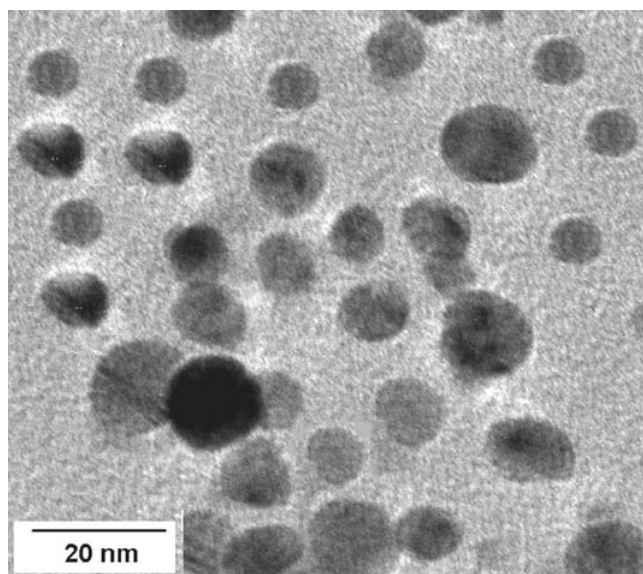


Figure 2. Transmission electron micrograph for specimen in figure 1.



Figure 1. Optical micrograph of a gel-derived $\text{Fe}(\text{NO}_3)_3\text{-SiO}_2$ film subjected to a d.c. voltage of 5 V and subsequently heated at 400 K for 2 h.

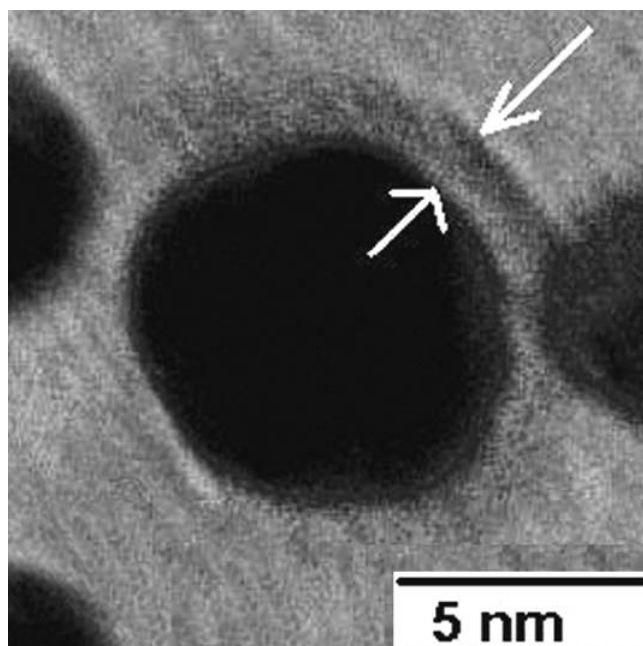


Figure 3. Transmission electron micrograph of the core-shell nanostructure.

e the electronic charge, c the ratio of $[\text{Fe}^{2+}]/[\text{Fe}]_{\text{total}}$, α^{-1} the localization length of the localized state at the Fe ion site and W the activation energy for hopping condition. The experimental data were least square fitted to (1) and the extracted parameters are $W = 0.66$ eV, $\alpha = 0.9 \text{ \AA}^{-1}$, $R = 2.9 \text{ \AA}$, $c = 0.9$ and $\nu_0 = 0.1 \times 10^{13} \text{ s}^{-1}$. These are typi-

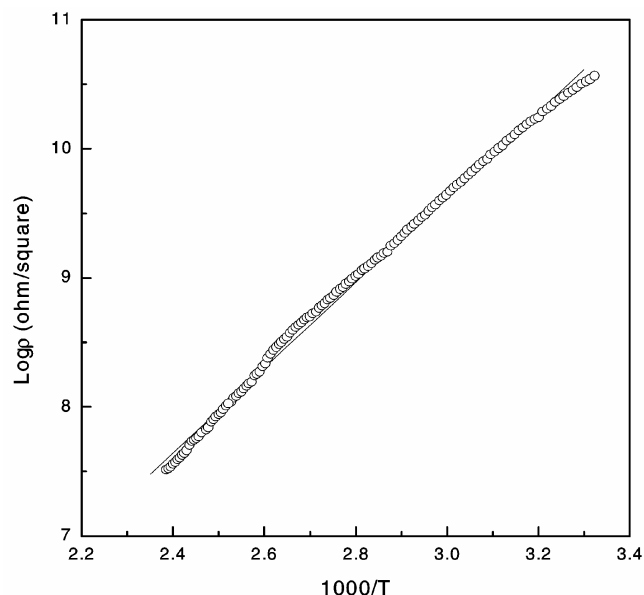


Figure 4. Variation of surface resistivity as a function of inverse temperature for the nanocomposite subjected to 2 h oxidation treatment.

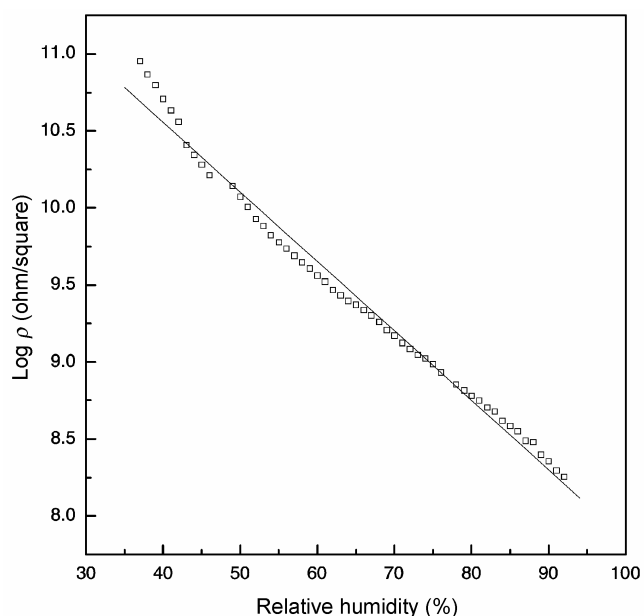


Figure 5. Surface resistivity variation as a function of relative humidity for specimen subjected to 2 h oxidation treatment.

cal for other samples and are consistent with the model used.

Figure 5 depicts the variation of the surface resistivity as a function of relative humidity in the case of specimen subjected to a 2 h oxidation treatment. This is typical of the other specimens. An almost three-order of magnitude resistivity change can be seen for the variation of relative humidity from 30 to 90%. The electrical conduction under humid conditions was found to be electronic in origin. This is believed to arise due to electron injection into the Fe_3O_4 phase by water molecules chemisorbed on Fe_3O_4 shells.

3.2 Gold-gold sulfide nanorods

Figure 7(a) is an electron micrograph for a Au_2S coated gold nanorod. Figure 7(b) is an electron diffraction pattern obtained from figure 7(a). The interplanar spacing, d_{hkl} values, were calculated from the measured diameters of the diffraction rings. In table 1, the experimentally determined d_{hkl} values have been compared with standard ASTM data for gold and gold sulfide phases, respectively. It is evident that both these phases are present in the samples prepared.

Figure 8 shows typical extinction coefficient variation as a function of wavelength in the case of a sample consisting of gold sulfide coated gold nanorods. Three main peaks can be seen as indicated by 1, 2 and 3 in the figure. The peaks 1 and 2 were explained as arising due to longitudinal and transverse modes of plasmon resonance, respectively of the gold nanorods. This was concluded by fitting the experimental data to the equation for extinction coefficient deduced by Gans (1915) on the basis of extended Mie theory. The peak number 3 was analysed on the basis of a core-shell structure of the rods (Zhou *et al* 1994). The small hump in the extinction coefficient described by 4 in figure 8 was ascribed to the presence of gold nanoparticles. It should be mentioned here that the gold nanorods as observed by transmission electron microscopy comprised of interconnection between numerous gold particles. The details of analysis have been published elsewhere (Chatterjee *et al* 2006).

Table 1. Comparison of d_{hkl} values obtained from electron diffraction with standard ASTM data for sulfide-coated gold nanorod.

Observed d_{hkl} (nm)	ASTM	
	Au (nm)	Au_2S (nm)
0.298		0.289 (111)
0.235	0.2355 (111)	
0.201	0.2039 (200)	
0.178		0.178 (220)
0.143	0.1442 (220)	

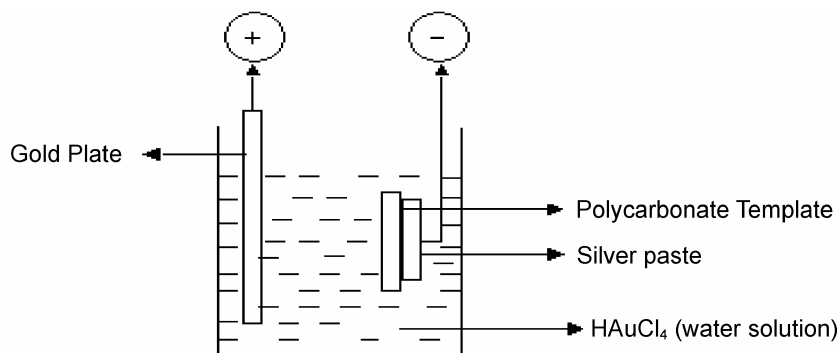


Figure 6. Experimental arrangement for growing gold nanowires.

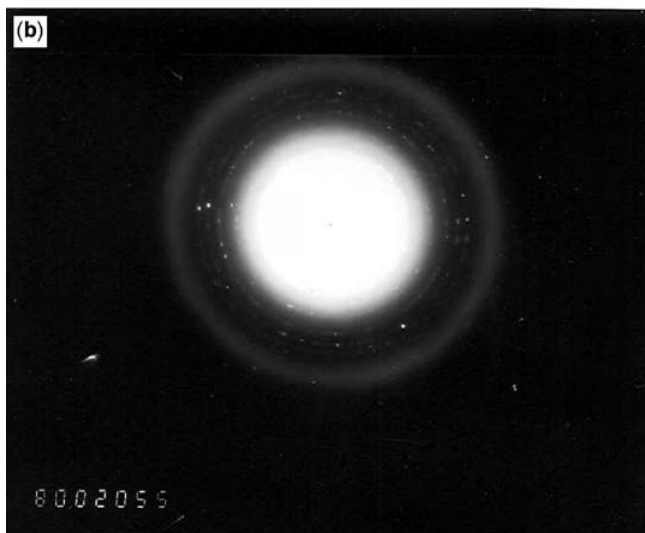
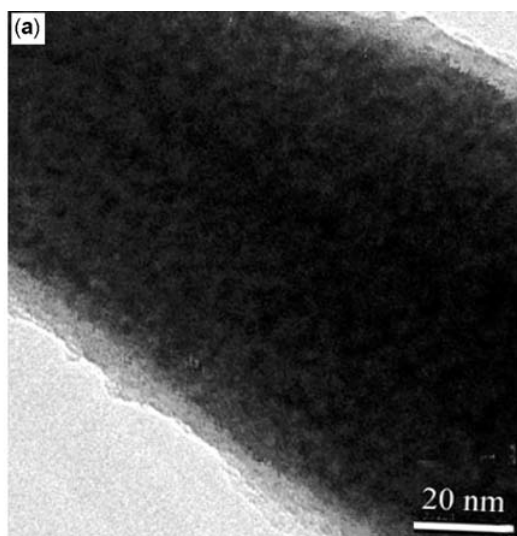


Figure 7. (a) Transmission electron micrograph for gold sulfide coated gold nanorod and (b) electron diffraction pattern obtained from figure 7(a).

3.3 Silver oxide and silver nanoparticles in polymer film

Figure 9 is a transmission electron micrograph of Ag_2O particles prepared here. The electron diffraction pattern

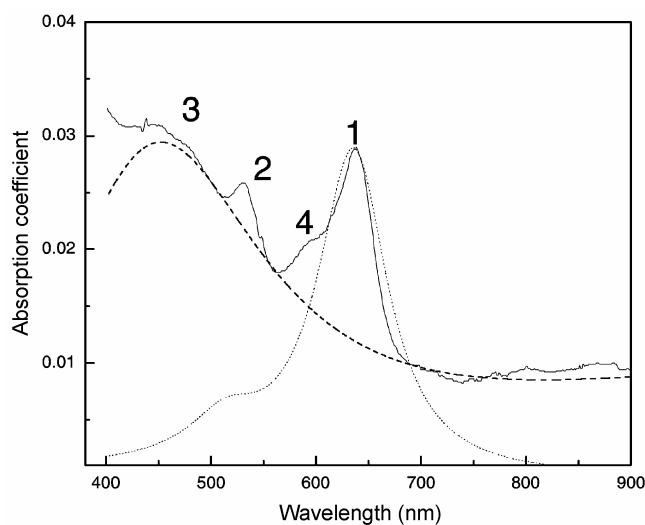


Figure 8. Optical absorption spectrum for gold sulfide coated gold nanorods as a function of wavelength at 300 K.

confirmed the particles to be made up of Ag_2O . Silver nanoparticles distribution was similar. On analysing the particle sizes by a log normal distribution function, the extracted values of median diameter and geometric standard deviation were found to be 8.5 nm and 1.2, respectively.

An a.c. field of 10 V/mm at a frequency of 50 Hz formed a string like structure parallel to the electrodes. Such a pattern formation is explained as arising due to electrohydrodynamic (EDH) fluid flow (Trau *et al* 1997).

Figure 10 shows the scanning electron micrograph for the binary nanoparticles under the influence of an a.c. field of 10 V/mm at a frequency of 1 MHz. The alignment of the particle arrays perpendicular to the electrodes has been explained on the basis of interaction energy between the dipoles associated with the nanoparticles. Using the expression for dipole-dipole interaction and the polarizabilities of particles it was found that the interaction energies $U_{\text{Ag-Ag}}$ and $U_{\text{Ag-Ag}_2\text{O}}$ were both negative but $U_{\text{Ag-Ag}}$ had a higher magnitude than $U_{\text{Ag-Ag}_2\text{O}}$ (Pal *et al* 2005). This explained the alignment of the particle arrays along the electric field direction.

Figure 11 gives the resistivity variation as a function of inverse temperature for a PMMA film containing the aligned binary particles. The higher temperature region shows resistivity variation controlled by the statistically distributed silver nanoparticle pairs between which electron hopping takes place—the silver particles forming localized states.

Figure 12 gives the variation of resistivity of the PMMA film containing aligned binary nanoparticles as a function of relative humidity—the frequency of the a.c. field being 100 KHz at which the alignment was brought about. It can be seen that the present system shows marked dependence of resistivity on relative humidity. This is

ascribed to an increase in the density of states resulting from the absorption of water molecules on the silver nanoparticles (Pal *et al* 2003).

3.4 Lead sulfide nanowires in mica channels

Figure 13(a) gives a dark field image of the transmission electron micrograph of PbS nanowires. In this figure the bright lines indicate the presence of nanowires. Figure 13(b) is the electron diffraction pattern obtained from

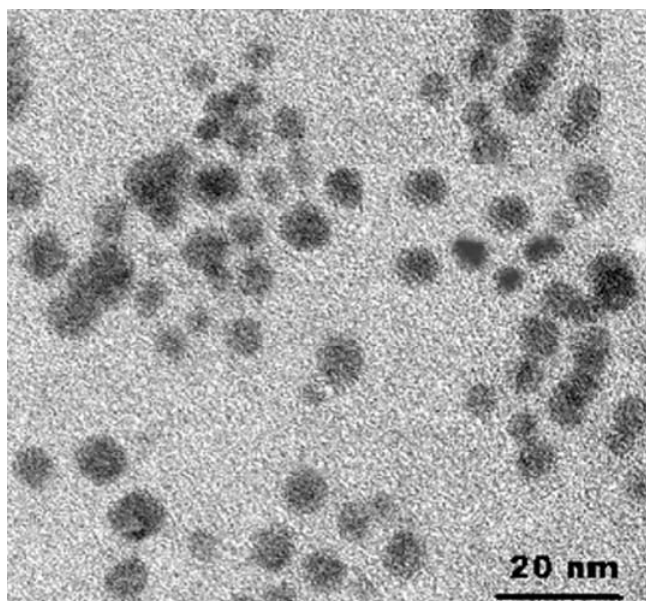


Figure 9. Transmission electron micrograph of Ag₂O particles.

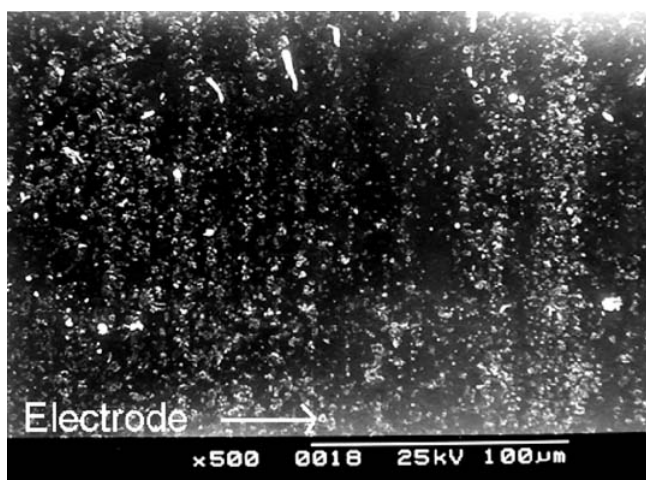


Figure 10. Scanning electron micrograph for the binary nanoparticles, Ag and Ag₂O.

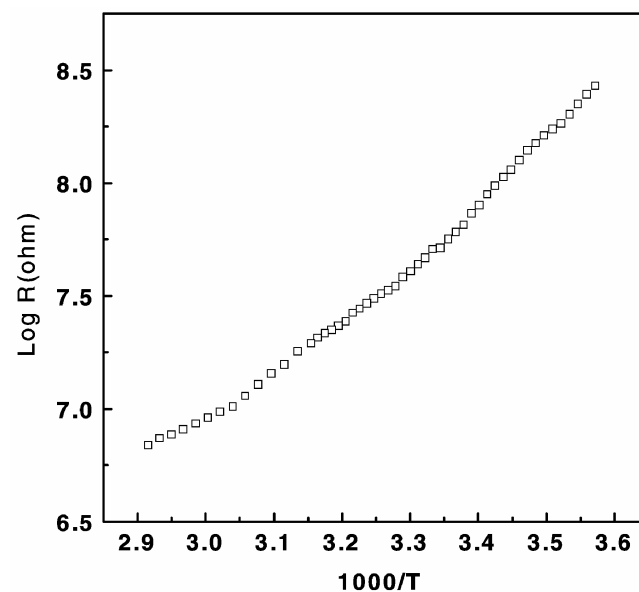


Figure 11. Variation of logarithm of resistance as a function of inverse temperature for PMMA film containing aligned binary nanoparticles of Ag and Ag₂O.

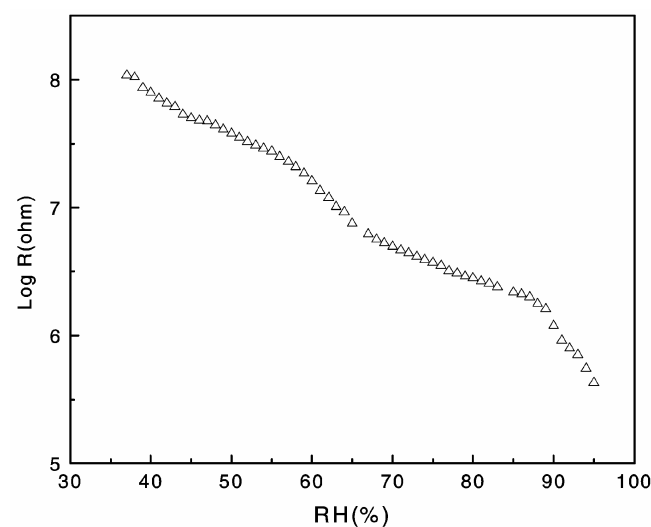


Figure 12. Variation of logarithm of resistance as a function of relative humidity for PMMA–binary nanoparticle composite aligned by a.c. field at 100 kHz.

figure 13(a). The interplanar spacings calculated from the diffraction spots confirm the presence of PbS in the nanowires. From figure 13(a) it should be evident that many of the nanowires have break-gaps.

Figure 14 shows the variation of resistance of a nanocomposite of PbS in Na-4 mica as a function of temperature. It can be seen that there is a transition from a semi-conducting state to a metallic state at around 300 K. The bandgap calculated from the slope of $\log R$ vs $1/T$ was found to be 0.32 eV which is consistent with the semi-

conducting phase, PbS. The transition to a metallic state at temperatures below 300 K has been ascribed to the effect of high pressure generated by the mismatch of thermal expansion coefficients of mica and PbS phases. A pressure of ~ 3.1 GPa was calculated due to the cooling of the sample from 673 K (synthesis temperature) to 300 K. The resistance change in the present system is, therefore, a direct consequence of a decrease in the bandgap with increasing pressure.

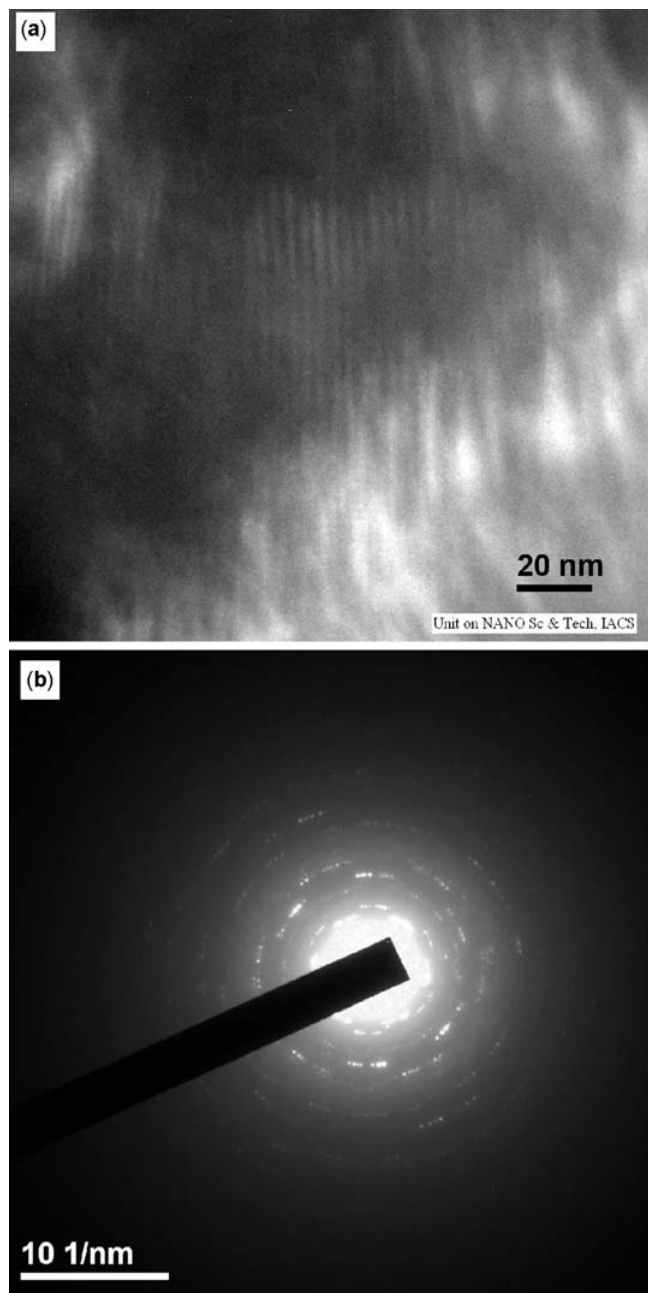


Figure 13. (a) Dark field image of transmission electron micrograph for PbS nano wires grown within Na-4 mica channels and (b) electron diffraction pattern obtained from figure 13(a).

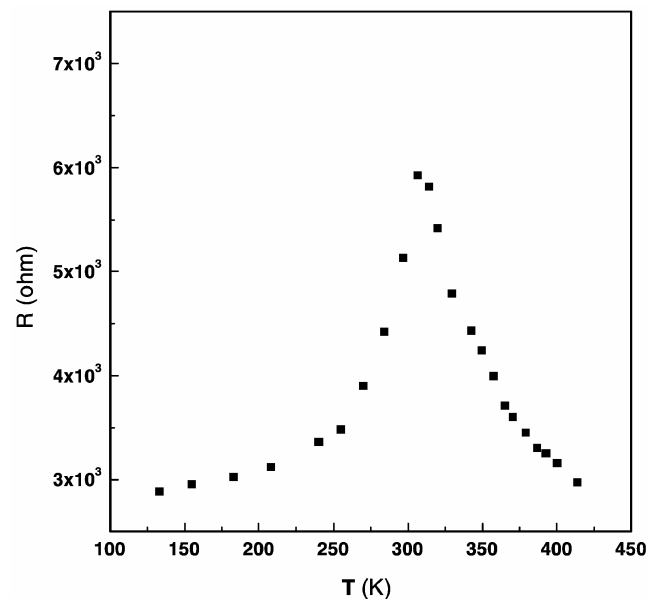


Figure 14. Resistance variation as a function of temperature for PbS/Na-4 mica nanocomposites.

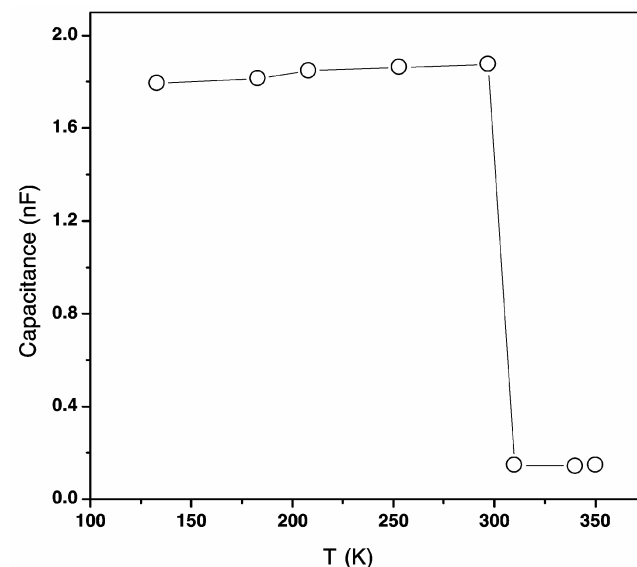


Figure 15. Variation of capacitance as a function of temperature for PbS/Na-4 mica nanocomposite.

The semiconductor–metal transition is further corroborated by the drastic increase in the capacitance value of the sample as the temperature is lowered below 300 K. Figure 15 depicts the variation of capacitance as a function of temperature for a nanocomposite comprising of Na-4 mica and PbS nanowires. It has been shown earlier that interrupted strands of metal should have high dielectric permittivity (Rice and Bernasconi 1972). In the present specimen system there are broken PbS nanowires of average length, ~ 20 nm (as estimated from electron micrographs). After they have undergone a transition to a metallic phase the predicted value of dielectric constant in accordance with Rice and Bernasconi (1972) model would be around 570. This is of the same order of magnitude as that calculated from the data in figure 15. Further details of the above analysis have been reported elsewhere (Mukherjee *et al* 2006a).

3.5 Copper sulfide nanowires in Na-4 mica channels

Figure 16 is a transmission electron micrograph for nanocomposite of Na-4 and copper sulfide nanowires. The diameters are seen to be ~ 1.2 nm. From electron diffraction spots we found that both CuS and Cu_2S were present in our system. Also there are segments of these nanowires present within the channels.

Figure 17 shows the variation of $\log R$ as a function of inverse temperature. The activation energy can be seen to be very small indicating transport by electron tunneling. It was reported earlier that CuS could exhibit metallic conduction (Gopalakrishnan *et al* 1979). We therefore conclude that CuS segments of diameter 17.4 nm (as deduced from X-ray line broadening of this phase) contribute to conduction by electron tunneling.

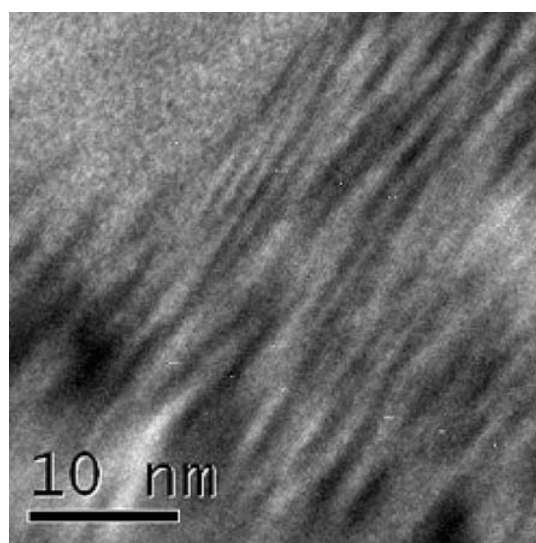


Figure 16. Transmission electron micrograph for a nanocomposite of Na-4 mica and copper sulfide nanowires.

Figure 18 shows the variation of capacitance of the Na-4 mica–copper sulfide nanocomposite as a function of frequency. The large value of dielectric permittivity, viz. 1617 as extracted from this result at high frequencies could be explained as arising due to Rice–Bernasconi mechanism explained earlier. The model predicted a value of 1682 in satisfactory agreement with the observed result.

The details of the above analysis have been discussed elsewhere (Mukherjee *et al* 2006b).

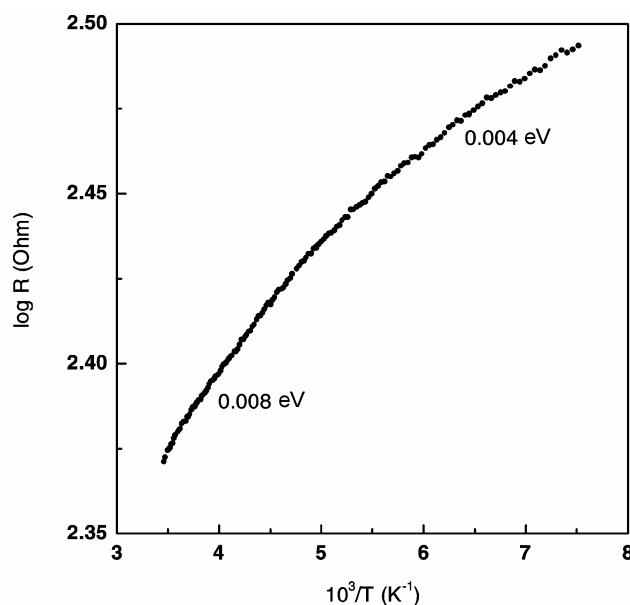


Figure 17. Variation of logarithm of resistance as a function of inverse temperature for a Na-4 mica–copper sulfide wire nanocomposite.

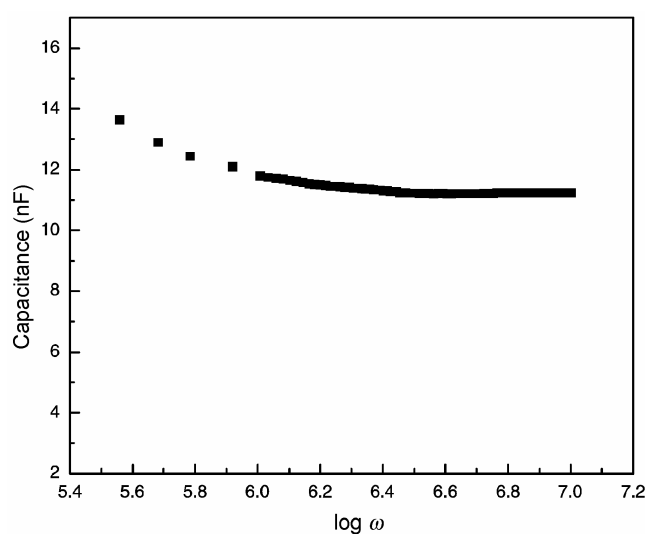


Figure 18. Variation of capacitance as a function of frequency for a Na-4 mica–copper sulfide wire nanocomposite.

3.6 Silver core–silver orthosilicate shell nanostructures

Figure 19 is a typical transmission electron micrograph for a glass containing silver nanoparticles and subjected to a heat treatment at 833 K for 1 h followed by 993 K for 2 h. From the figure it can be seen that the silver core has a diameter of ~ 20 nm and the orthosilicate shell a thickness of ~ 21 nm. The electron diffraction pattern confirms the presence of silver orthosilicate shell.

Figure 20 shows the variation of logarithm of d.c. resistance as a function of inverse temperature for a glass sample containing silver–silver orthosilicate core-shell nanostructure. It can be seen from this figure that at tem-

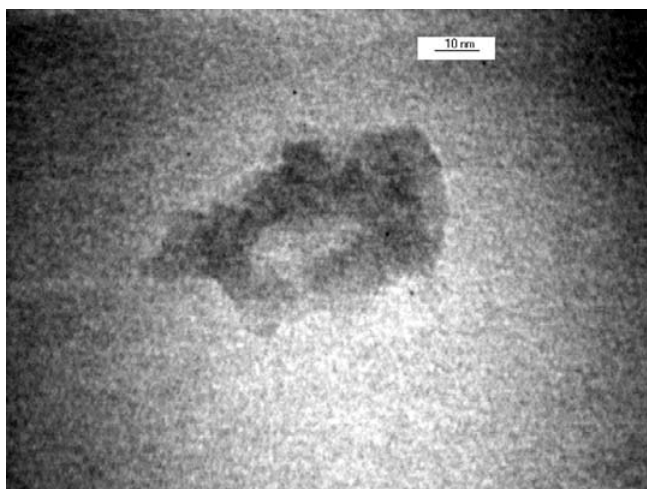


Figure 19. Transmission electron micrograph for a glass containing core-shell structure of silver nanoparticles and silver orthosilicate layers.

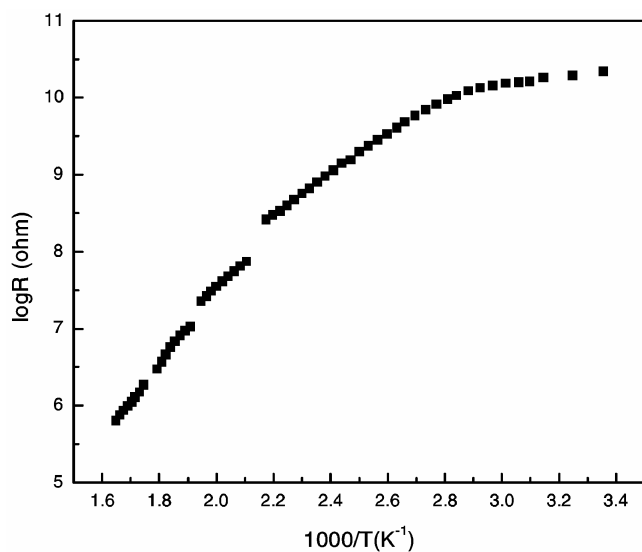


Figure 20. Variation of logarithm of d.c. resistance as a function of inverse temperature for a glass containing silver–silver orthosilicate core-shell nanostructure.

peratures around 460 K, 510 K and 570 K, the resistance shows discontinuous changes. This behaviour has been explained on the basis of high pressure generated on the shell phase due to thermal expansion mismatch between silver core and oxide shell. This causes a deformation in the shell perimeter and whenever it reaches a value equal to Si–O distance (*viz.* 0.16 nm), sharp change in resistance occurs. Considering the expression for electrical conductivity for an ionically conducting material, the pre-exponential factor contains the term, ν , which is the ionic vibrational frequency. According to Lamb's (1882) theory, the spheroidal acoustic modes are quantized in terms of their frequencies. The present data were analysed on the basis of this theory and it was shown that the discontinuous changes in conductivity were a direct consequence of the excitation of Lamb modes (Ghosh *et al* 2004).

3.7 Iron–iron oxide core-shell nanostructure and optical properties

Figure 21 is a transmission electron micrograph showing the core-shell structure of a nanocomposite which was given an oxidation treatment at 573 K for 30 min. The histogram of particle sizes showed a median diameter of 5.3 nm. From electron diffraction pattern of the core-shell structure it was concluded that both α -Fe and Fe_3O_4 were present.

Figure 22 shows the variation of optical absorption as a function of wavelength for the nanocomposite which was given a heat treatment at 873 K for 30 min. It is evident that there are three absorption peaks in the figure. The first one arises due to the presence of uncoated iron nanoparti-

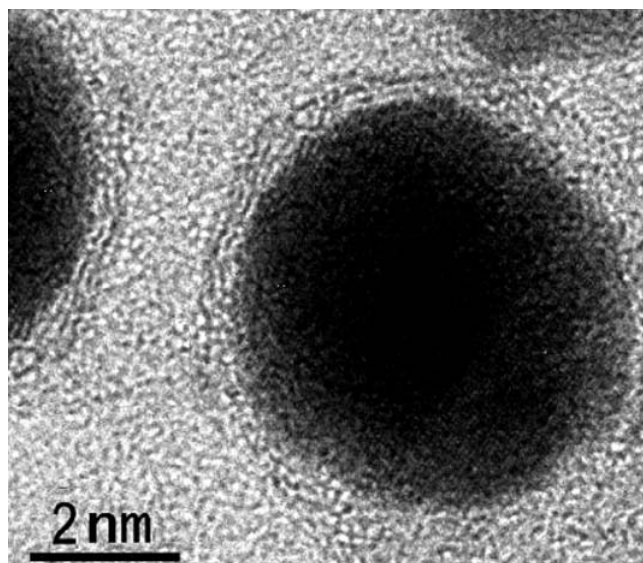


Figure 21. Transmission electron micrograph of an iron core–iron oxide shell nanostructure in a glass medium.

cles and is analysed by applying Maxwell–Garnet model (Maxwell–Garnet 1904) according to which the effective permittivity of the medium, $\bar{\epsilon}$, can be written as

$$\bar{\epsilon} = \frac{2f\epsilon_m\epsilon_h - 2f\epsilon_h^2 + \epsilon_m\epsilon_h + 2\epsilon_h^2}{\epsilon_m + 2\epsilon_h - f\epsilon_m + f\epsilon_h}, \quad (2)$$

where f is the volume fraction of the metallic phase, ϵ_m the dielectric permittivity of the latter and ϵ_h the dielectric permittivity of the host medium (in our case silicate glass). The expression for ϵ_m is as given below (Kreibig 1974)

$$\epsilon_m = 1 - \frac{\omega_p^2}{\omega^2 - i\omega\sigma/\epsilon_0}, \quad (3)$$

where ω_p is the plasmon frequency for iron, σ the conductivity of iron particle and ϵ_0 the free space permittivity. The calculated value of plasmon frequency of iron is 2.3×10^{16} rad/s (Kittel 1961). The optical absorption coefficient, μ , is given by (Chatterjee *et al* 1989)

$$\mu = \frac{\omega}{c} \frac{\bar{\epsilon}_2}{\sqrt{\bar{\epsilon}_1}}, \quad (4)$$

where ω is the angular frequency, c the velocity of light, $\bar{\epsilon}_1$ and $\bar{\epsilon}_2$ are the real and imaginary parts, respectively of $\bar{\epsilon}$.

The first peak was fitted to (2), (3) and (4) taking σ , f and ϵ_h as parameters. In the figure the dotted line represents the theoretical fit and the solid line corresponds to experimental data. The values extracted for the parameters were $\sigma = 3.9 \times 10^4$ (ohm m) $^{-1}$, $f = 1 \times 10^{-3}$ and $\epsilon_h = 3.8$. These values are reasonable for our system.

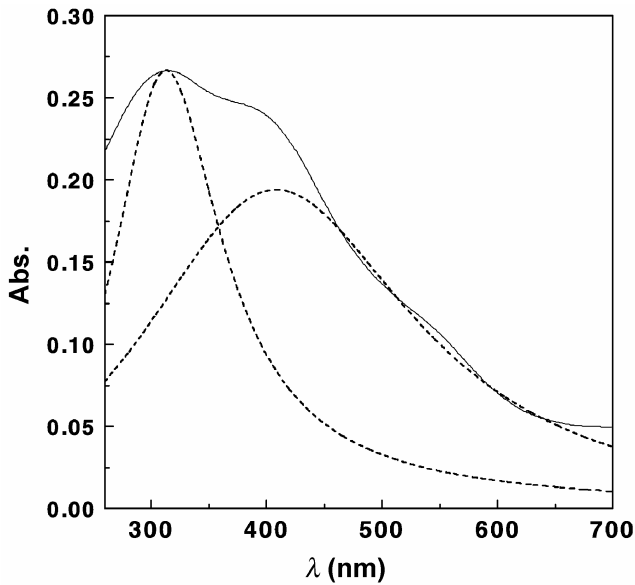


Figure 22. Optical absorption as a function of wavelength for a nanocomposite with iron core–iron oxide shell nanostructure.

The second peak was analysed on the basis of the presence of core-shell structured nanoparticles. The polarizability, α , in this case can be written as (Zhou *et al* 1994)

$$\alpha = \sum_j \frac{n_j r_j^3}{\sum_j n_j r_j^3} \left\{ \frac{(\epsilon_s - \epsilon_h)(\epsilon_{mj} + 2\epsilon_s) + \left(1 - \frac{t_j}{r_j}\right)^3}{(\epsilon_{mj} - \epsilon_s)(\epsilon_h + 2\epsilon_s)} \right\} r_j^3, \quad (5)$$

where ϵ_s is the dielectric permittivity of the shell, n_j the number of particles having radius r_j and t_j the thickness of the shell on the particle r_j . The size dependent dielectric permittivity, ϵ_{mj} , for a metal core with radius, r_j , is given by (Kreibig 1974)

$$\epsilon_{mj} = \left(1 - \frac{\omega_p^2}{\omega^2}\right) + i \left[\frac{\omega_p^2}{\omega^3} \left(\frac{\sigma_{mj}}{\epsilon_0} + \frac{V_F}{r_j - t_j} \right) \right], \quad (6)$$

where σ_{mj} is the electrical conductivity of the metal core with radius ($r_j - t_j$), ϵ_0 the free space permittivity and V_F the Fermi velocity for iron. Using Clausius–Mosotti relation (Kittel 1961), the dielectric permittivity of the composite system can be written as

$$\alpha = \frac{1 + 2N\alpha}{1 - N\alpha}, \quad (7)$$

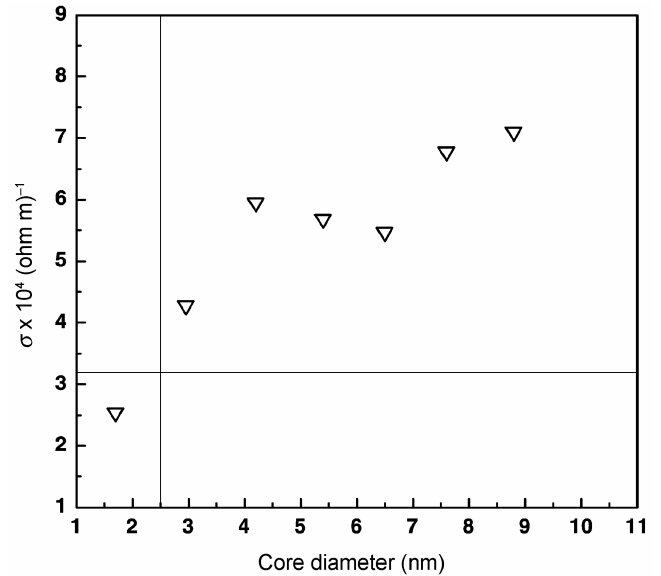


Figure 23. Extracted values of electrical conductivity as a function of iron particle diameter in the case of sample heat treated at 873 K for 30 min.

where N is the number of nanoparticles per unit volume. Using (5), (6) and (7), the second peak was fitted using N , ε_s , t_j and σ_{mj} as the variable parameters. The dotted line in figure 22 shows the theoretical fit. The values of σ_{mj} as extracted from the fitting are summarized in figure 23. It can be seen that for core diameter of metallic iron below

~ 2.5 nm the conductivity values extracted by this fitting procedure fall below Mott's minimum metallic conductivity which is given by

$$\sigma_{\min} \cong \left(\frac{0.06e^2}{\hbar a} \right) \left(\frac{6}{z} \right)^2, \quad (8)$$

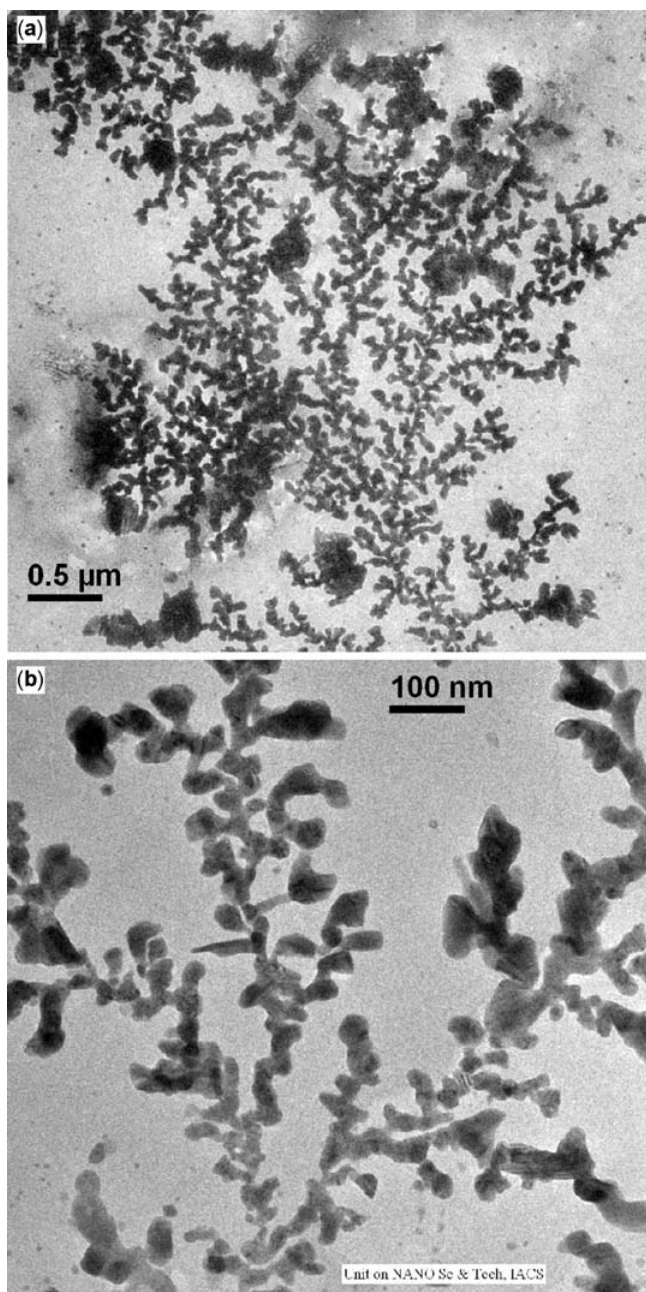


Figure 24. Transmission electron micrograph of dendron-like growth of silver particles using tetrapeptide at different magnifications: (a) scale bar, 0.5 μm and (b) scale bar, 100 nm. (Reprinted figure with permission from Santanu Bhattacharya, Apurba K Das, Arindam Banerjee and Dipankar Chakravorty 2006 *J. Phys. Chem.* **B110** 10758; Copyright @ American Chemical Society (2006)).

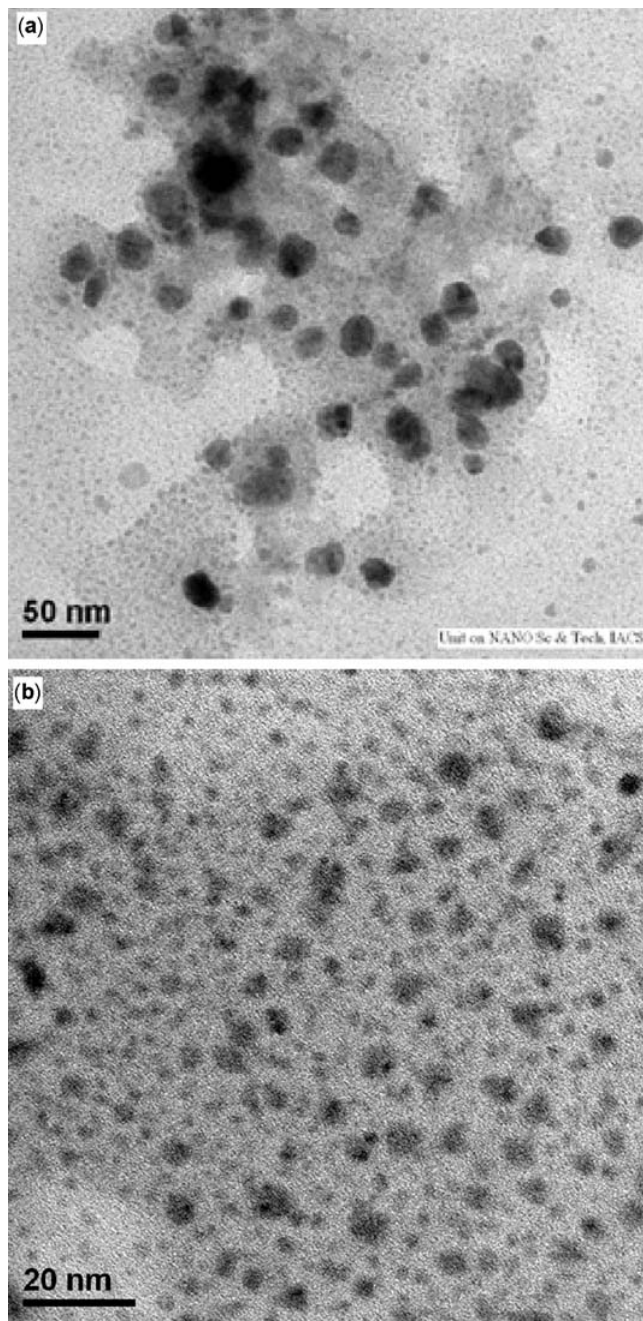


Figure 25. Nanoparticles of silver in the peptide solution: (a) scale bar, 50 nm and (b) scale bar, 20 nm. (Reprinted figure with permission from Santanu Bhattacharya, Apurba K Das, Arindam Banerjee and Dipankar Chakravorty 2006 *J. Phys. Chem.* **B110** 10758; Copyright @ American Chemical Society (2006)).

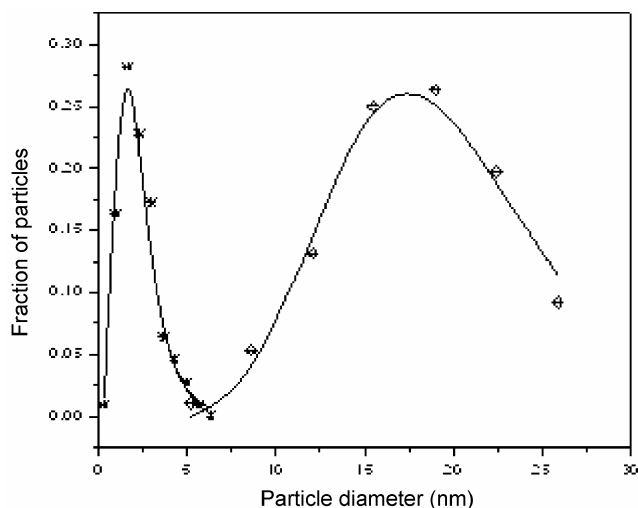


Figure 26. Particle size distribution obtained from figure 25.

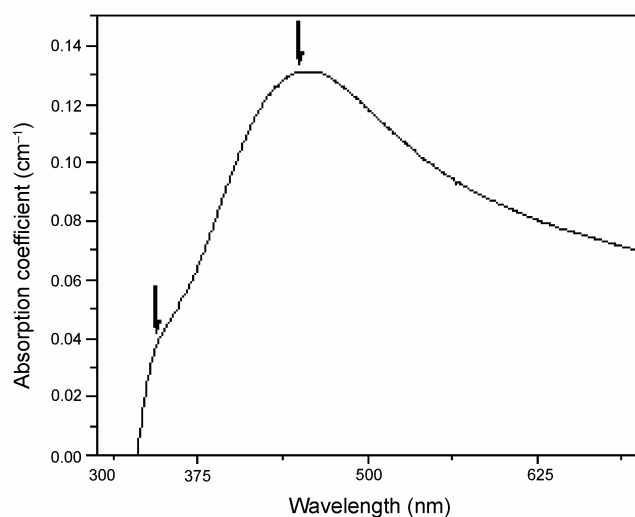


Figure 27. Optical absorption spectra for silver nanoparticles synthesized for a duration of 4 h.

where e is the electronic charge, \hbar the Planck's constant, ' a ' the interatomic distance and z the coordination number. For the present system the calculated value of σ_{\min} is $\sim 3.2 \times 10^4 (\Omega\text{m})^{-1}$. The third peak at 550 nm is explained to arise due to $d-d$ transition (Jitianu *et al* 2002).

3.8 Silver nanoparticles in oligopeptide

Figures 24(a) and (b) are the transmission electron micrographs of the dendron-like structure formed by silver nanoparticles. Figures 25(a) and (b) are electron micrographs at a higher magnification showing the silver particle size distribution. In figure 26 is shown the particle size distribution. It is seen that a bi-modal distribution

Table 2. Summary of extracted values of electrical conductivity for metallic silver for different values of particle diameter.

Particle diameter (nm)	Conductivity ($\Omega^{-1} \text{m}^{-1}$)
0.5	0.5
1	0.7
1.5	0.8
2	1.2
2.5	1.8
3	2.4
3.5	3.0
4	3.4
4.5	3.8
5	4.3
8.6	2.3
12	2.5
15.5	2.5
18.9	2.6
22.4	2.8

has been obtained, the mean diameters being 2 nm and 19.5 nm, respectively. This is reflected in the optical absorption spectra shown in figure 27 where two peaks are observed—the peak at 340 nm is due to particles with a median diameter, 2 nm and the peak at 450 nm arises due to those with a median diameter, 19.5 nm. This has been confirmed by analysing the absorption data on the basis of Mie scattering theory (Mie 1908) according to which the absorption coefficient, η , is given by

$$\eta = \sum_j \frac{18\pi f_j \epsilon_m^{3/2} \epsilon_{2j}}{\lambda [(\epsilon_{1j} + 2\epsilon_m)^2 + \epsilon_{2j}^2]}, \quad (9)$$

where f_j is the volume fraction of particles with diameter, d_j , ϵ_m the dielectric constant of the medium (methanol in our case) and ϵ_{1j} and ϵ_{2j} are the real and imaginary parts of the dielectric permittivity of the metal particle with diameter, d_j . The size dependent dielectric permittivity of a metal particle was calculated by (6). The experimental data of absorption coefficient were satisfactorily fitted to (9) and (6) using σ_j , f and ϵ_m as parameters. The extracted values of conductivity for different particle diameters are summarized in table 2. It can be seen from these values that below a particle diameter of 2 nm, the conductivities have values below Mott's minimum metallic conductivity which in the present case was calculated using (8) to be $1.2 \times 10^4 (\text{ohm})^{-1}$.

Acknowledgements

The work was supported by DST, New Delhi, under Nano Science and Technology Initiative Programme, S Basu, B N Pal, P K Mukherjee, B Ghosh, K Chatterjee, A Bose and S Bhattacharya thank CSIR, New Delhi, for awarding Senior Research Fellowships. (DC) thanks INSA, New

Delhi, for the award of a Senior Scientist position. The authors thank Supriyo Chakravorty for providing skillful assistance in transmission electron microscopy.

References

- Banerjee Sourish, Banerjee Soomit, Datta Anindya and Chakravorty Dipankar 1999 *Europhys. Lett.* **46** 346
- Basu S and Chakravorty D 2006 *J. Non-Cryst. Solids* **352** 380
- Bhattacharya Santanu, Das Apurba K, Banerjee Arindam and Chakravorty Dipankar 2006 *J. Phys. Chem.* **B110** 10757
- Bodanszky M and Bodanszky A 1984 *The practice of peptide synthesis* (New York: Springer-Verlag) pp 1–282
- Chatterjee A and Chakravorty D 1989 *J. Phys.* **D22** 1386
- Chatterjee K, Basu S and Chakravorty D 2006 *J. Mater. Res.* **21** 34
- Dutta P, Manivannan A, Seehra M S, Shah N and Huffman G P 2006 *J. Appl. Phys.* **99** 08H105
- Gans R 1915 *Ann. Phys.* **47** 270
- Ghosh B, Banerjee S, Ghosh A and Chakravorty D 2004 *Phys. Rev.* **B70** 195414
- Gopalakrishnan J, Murugesan T, Hegde M S and Rao C N R 1979 *J. Phys.* **C12** 5255
- Jitianu A, Crisan M, Megha A, Aru I and Zaharescu M 2002 *J. Mater. Chem.* **12** 1401
- Kesanli B, Hong K, Meyer K, Im H-J and Dai S 2006 *Appl. Phys. Lett.* **89** 214104
- Kittel C 1961 *Introduction to solid state physics* (New York: Wiley) p. 374
- Kodama T and Komarneni S 1999 *J. Mater. Chem.* **9** 533
- Kreibig U 1974 *J. Phys. F: Met. Phys.* **4** 999
- Lamb H 1882 *London Math. Soc.* **13** 189
- Matshushita M, Hond K, Toyoki H, Hayakawa Y and Kondo H 1986 *J. Phys. Soc. Jpn* **55** 2618
- Maxwell–Garnet J C 1904 *Trans. R. Soc. London* **A203** 385
- Mie G 1908 *Ann. Phys.* **25** 377
- Mott N F 1968 *J. Non-Cryst. Solids* **1** 41
- Mukherjee P K, Chatterjee K and Chakravorty D 2006a *Phys. Rev.* **B73** 035414
- Mukherjee Pijush Kanti, Bose Anindita and Chakravorty Dipankar 2006 *Appl. Phys. Lett.* **89** 033101
- Ng C Y, Chen T P, Ding L, Liu Y, Tse M S, Fung S and Dong Z L 2006 *Appl. Phys. Lett.* **88** 063103
- Pal B N, Kundu T K, Banerjee S and Chakravorty D 2003 *J. Appl. Phys.* **93** 4201
- Pal B N, Basu S and Chakravorty D 2005a *J. Appl. Phys.* **97** 034311
- Pal B N, Basu S and Chakravorty D 2005b *J. Appl. Phys.* **98** 084306
- Park J H and Park O O 2006 *Appl. Phys. Lett.* **89** 193101
- Rice M J and Bernasconi J 1972 *Phys. Rev. Lett.* **29** 113
- Trau M, Saville A and Aksay I A 1997 *Langmuir* **13** 6375
- Watt A, Eichmann T, Rubinsztein-Dunlop H and Meredith P 2005 *Appl. Phys. Lett.* **87** 253109
- Zhou H S, Honma I, Komiyama H and Haus J W 1994 *Phys. Rev.* **B50** 12052